Role of ocean heat transport in climates of tidally locked exoplanets around M dwarf stars

Yongyun Hu[1] and Jun Yang

Laboratory for Climate and Atmosphere–Ocean Studies, Department of Atmospheric and Oceanic Sciences, School of Physics, Peking University, Beijing 100871, China

Edited by Robert E. Dickinson, The University of Texas at Austin, Austin, TX, and approved November 22, 2013 (received for review August 13, 2013)

The distinctive feature of tidally locked exoplanets is the very uneven heating by stellar radiation between the dayside and nightside. Previous work has focused on the role of atmospheric heat transport in preventing atmospheric collapse on the nightside for terrestrial exoplanets in the habitable zone around M dwarfs. In the present paper, we carry out simulations with a fully coupled atmosphere–ocean general circulation model to investigate the role of ocean heat transport in climate states of tidally locked habitable exoplanets around M dwarfs. Our simulation results demonstrate that ocean heat transport substantially extends the area of open water along the equator, showing a lobster-like spatial pattern of open water, instead of an "eyeball." For sufficiently high-level greenhouse gases or strong stellar radiation, ocean heat transport can even lead to complete deglaciation of the nightside. Our simulations also suggest that ocean heat transport likely narrows the width of M dwarfs' habitable zone. This study provides a demonstration of the importance of exooceanography in determining climate states and habitability of exoplanets.

planetary climate | exoplanet habitability | superEarth

M dwarf stars are the most common type of star in the Universe (1). The habitable zone (HZ) around M stars is close to such stars because of their weak luminosity (2). In consequence, habitable exoplanets orbiting M stars are likely to be tidally locked to their primary stars, so that one side of tidal-locking exoplanets permanently faces stars, and the other side remains dark. Previous studies have demonstrated the role of atmospheric heat transport in preventing atmospheric collapse on the nightside of terrestrial exoplanets located in the HZ of M stars (3–10). For a planet with an extensive ocean, its climate and habitability also involves ocean heat transport, which is known to be important in Earth's climate (11). None of the existing studies has considered the role of ocean heat transport. Moreover, the climate also involves the spatial distribution of open water versus ice and the question of whether the planet becomes locked in a globally glaciated Snowball state. Simulation with a comprehensive Earth atmospheric general circulation model (AGCM) coupled to a slab ocean, without dynamic ocean heat transport, revealed an "eyeball" climate state, with a round area of open ocean centered at the substellar point and complete ice coverage on the nightside, even for very high CO_2 concentrations (4). In the presence of sea ice, ocean heat transport is likely to be especially important, because it is known from studies of the Snowball Earth phenomenon in Earth-like conditions that ocean heat transport is very effective in holding back the advance of the sea-ice margin (12–14). The distribution of sea ice on tidally locked exoplanets is only an issue for M stars, because planets with sufficiently dense atmospheres orbiting hotter stars in orbits close enough to yield tidal locking are likely to be too hot to permit ice and may even be too hot to retain water. The purpose of the present paper is to study how ocean heat transport and sea-ice processes influence the climate and habitability of tidal-locking exoplanets in the HZ around M stars by carrying out simulations with a fully coupled atmospheric–oceanic general circulation model (AOGCM).

Methods

The AOGCM used here is the Community Climate System Model version 3 (CCSM3) (15), which was originally developed at the National Center for Atmospheric Research for studying Earth climate. The model includes a dynamic ocean with both wind-driven and deep-ocean circulations. The sea-ice component of CCSM3 consists of energy-conserving thermodynamics and elastic–viscous–plastic dynamics, and the model freezing point of sea water is set to −1.8 °C. The atmosphere component has 26 vertical levels from the surface to the model top of 2.6 hPa and horizontal resolution of 3.75 by 3.75° in latitude and longitude. The ocean component has 25 vertical levels, longitudinal resolution of 3.6°, and variable latitudinal resolutions of about 0.9° near the equator. Eddy parameterization used in the ocean model is the Gent–McWilliams parameterization (16).

The model is modified with planetary parameters the same as that of Gliese 581g (Gl 581g) (17). The synchronous rotating period, radius, gravity, and incident stellar radiation are 36.7 Earth days, 1.5 times Earth radius, 13.5 m s^{-2}, and 866 W m^{-2}, respectively. Although Gl 581g is not a confirmed exoplanet, its planetary parameters represent a hypothetical Super-Earth in the HZ of an M star. The stellar spectrum used here is an M star spectrum, with an effective temperature of 3,400 K. Unlike the solar spectrum, most of the M star luminosity is emitted in the near-infrared. Near-infrared radiation is much less reflected by ice and snow compared with visible light. Thus, ice–albedo feedback is weaker on exoplanets orbiting M stars than on Earth (18). Here, sea ice and snow albedos are set to 0.3 and 0.6, respectively. The substellar point is located at the equator and 180° in longitude, and both the eccentricity and obliquity are set to zero. The geothermal heat flux is also set to zero. We assume that the exoplanet is an aquaplanet with a uniform ocean depth of 4,000 m, which is the mean depth of Earth's oceans.

The influence of CO_2 concentration on climate is probed with five different CO_2 levels: 3.6, 355, 10,000, 100,000, and 200,000 ppmv. It has been speculated that the atmosphere of aquaplanets could have high CO_2 levels because silicate weathering could be ceased by water coverage (19). On the other hand, it has been conjectured that CO_2 concentrations high enough to

Significance

Tidal-locking planets receive very uneven stellar heating because their one side permanently faces their stars and the other remains dark. While the dayside can be warm enough to sustain liquid water, the nightside could be so cold that any gases would condense out. Here, we perform simulations with a coupled atmosphere–ocean model to demonstrate the importance of exooceanography in determining the habitability of tidal-locking exoplanets around M dwarfs. We show that ocean heat transport can substantially extend the dayside habitable area and efficiently warm the nightside, so that atmosphere collapse does not occur. As greenhouse effect or stellar radiation is sufficiently strong, ocean heat transport can even cause global deglaciation. Ocean heat transport also likely narrows the width of M dwarfs' habitable zone.

Author contributions: Y.H. and J.Y. designed research; Y.H. and J.Y. performed research; Y.H. and J.Y. analyzed data; and Y.H. wrote the paper.

The authors declare no conflict of interest.

This article is a PNAS Direct Submission.

Freely available online through the PNAS open access option.

[1]To whom correspondence should be addressed. E-mail: yyhu@pku.edu.cn.

This article contains supporting information online at www.pnas.org/lookup/suppl/doi:10.1073/pnas.1315215111/-/DCSupplemental.

maintain open water in the outer portions of the HZ might be incompatible with limitations imposed by sea-floor weathering (12). All other atmospheric compositions are kept the same as present-day Earth. The radiative transfer module of the model is approximately valid for atmospheres with CO_2 concentration lower than 200,000 ppmv and water-vapor column amount less than 1,200 kg m^{-2}, although the simulated climate is very slightly colder than it should be (20, 21). For CO_2 levels above 200,000 ppmv, the effects of pressure broadening and collision-induced CO_2 absorption become significant (22, 23). In addition, we also examine climate states for exoplanets closer to both inner and outer edges of the HZ by performing simulations with a sequence of stellar radiation fluxes of 700, 866, 1,200, and 1,400 W m^{-2} and with constant CO_2 concentration of 355 ppmv.

The model is initialized with present-day Earth atmosphere conditions and globally uniform vertical profiles of present-day Earth ocean temperature and salinity. All AOGCM simulations are run for about 2,200 Earth years, and the results shown here are based on averages over the last 100 y. To distinguish the role of ocean heat transport, we also carry out simulations with an AGCM coupled with a 50-m slab ocean. The AGCM used here is the atmospheric component of the AOGCM. All AGCM simulations are run for 80 Earth years. Results shown here are averaged over the last 5 y.

Results

Fig. 1*A* shows AOGCM simulation results of sea-ice fraction and wind velocity at the lowest model layer for 355 ppmv of CO_2. This level of CO_2 roughly equals the present-day CO_2 concentration in the Earth atmosphere. In the presence of a dynamic ocean, the open-ocean area (blue) is not like the round iris of an "eye" such as that in AGCM simulations coupled with a slab ocean (Fig. S1*A*; also figure 3 in ref. 4). Instead, the spatial pattern of the open-ocean region is more like a "lobster," showing two "claws" symmetric to the equator and a long tail along the equator. The tail of open water extends eastward to the nightside. At the western side of the substellar point, sea ice is drifted eastward from the nightside toward the substellar point. The open-ocean region remains even for 3.6 ppmv of CO_2 and shows the similar lobster-like spatial pattern. For very high-level CO_2 (200,000 ppmv), sea ice is completely melted (Fig. 1*B*). By contrast, the nightside and a large part of the dayside remain frozen for the same level of CO_2 in the AGCM simulation (Fig. S1*B*), and the open-ocean region is only slightly expanded compared with that in Fig. S1*A*.

Spatial distributions of surface air temperatures (T_s) (color shading) and surface ocean velocity (arrows) are illustrated in Fig. 1 *C* and *D*. For 355 ppmv CO_2, the highest T_s is not located at the substellar point but has two centers at each side of the equator with values of about 5–6 °C. This is because the eastward equatorial ocean current transports cold water from the dark side to the dayside. The lowest T_s is not located at either pole or the antistellar point but at subpolar regions of the nightside with values of about −60 °C. The lowest T_s is well above the condensation temperature of CO_2 (−78.5 °C at 1 bar of CO_2 partial pressure and much lower at lower partial pressures), so there is no risk of CO_2 being trapped in the cold regions. As CO_2 concentration is increased to 200,000 ppmv (Fig. 1*D*), the highest T_s on the dayside does not rise very much, only about 2 or 3 °C. However, nightside and polar surface temperatures increase drastically and are all above the freezing point of ocean water. Thus, temperature contrasts between the dayside and nightside and between the tropics and poles are largely reduced. Comparison between Fig. 1*D* and Fig. S1*D* reveals that as CO_2 concentration is sufficiently high, ocean heat transport is very efficient in warming the nightside and causing sea-ice melting there.

The flow pattern in Fig. 1 is the well-known Gill-type solution responding to a stationary equatorial heating source (24). The two cyclones at each side of the equator are the tropical Rossby-wave modes, and the eastward long tail along the equator is the tropical Kelvin wave. Similar flow patterns have been seen in atmospheric flows in previous simulation studies for tidally locked terrestrial exoplanets and hot Jupiters (e.g., 5–7, 10, 25, 26). Both the simulations for 355 and 200,000 ppmv CO_2 show a strong westerly equatorial ocean current on the order of a few meters per second. The equatorial westerly ocean current is mainly driven by westerly winds as demonstrated in ref. 27, although the tropical Kelvin and Rossby waves also contribute to the formation of the ocean current. This is different from the equatorial westerly atmospheric flow of tidal-locking exoplanets, which is driven by equatorward convergence of Rossby-wave momentum fluxes (10, 25, 26). The reason why the equatorial ocean current is so strong is because there are no meridional continental barriers and the wind-driven ocean current can be very strong (28, 29). The equatorial current here is just like the

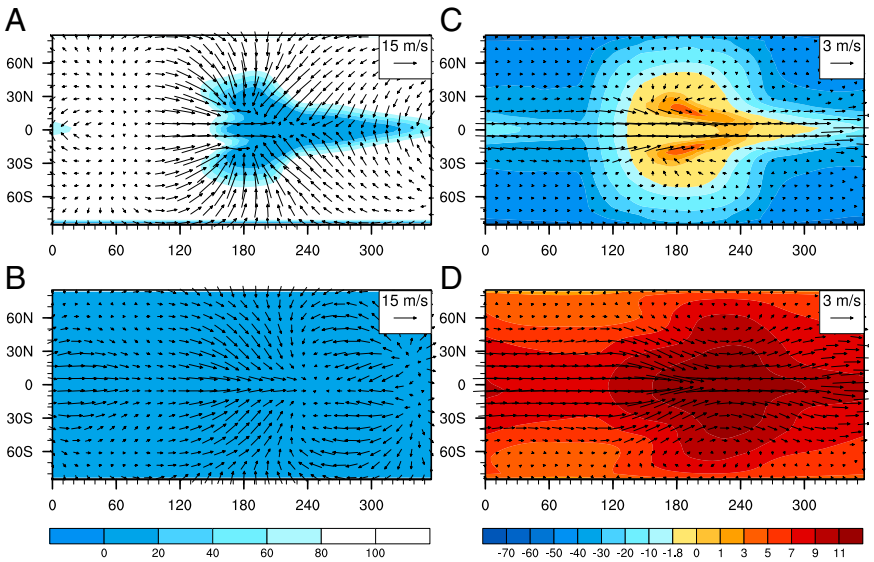

Fig. 1. Spatial distributions of sea-ice fraction and surface air temperature. (*Left*) Sea-ice fraction (unit, %); (*Right*) surface air temperature (unit, °C); (*Upper*) 355 ppmv CO_2; and (*Lower*) 200,000 ppmv CO_2. In *A* and *B*, arrows indicate wind velocity at the lowest level of the atmospheric model (990 hPa), with a length scale of 15 m s^{-1}. In *C* and *D*, arrows indicate ocean surface current velocity, with a length scale of 3 m s^{-1}. Note that the color scale for surface air temperature is not linear. The substellar point is at the equator and 180° in longtitude.

strong Antarctic Circumpolar Current in the Southern Ocean of Earth. Ocean currents, especially the equatorial jet stream, become stronger with increasing CO_2 (Fig. 1*D*). This is because the open-ocean area becomes broader with increasing CO_2, so that wind stresses can force on the broader open-ocean surface and generate stronger zonal ocean currents.

Thermal structures and motions of deep-ocean layers also play important roles in ocean heat transports. Fig. 2 illustrates depth–latitude cross-sections of zonal-mean ocean potential temperatures and zonal velocities for 355 and 200,000 ppmv CO_2, respectively. For 355 ppmv CO_2, the relatively warm layer (higher than −1.8 °C) is limited in the tropics and above 400 m in depth (Fig. 2*A*), whereas all other parts of the ocean show rather homogeneous temperature distribution. For 200,000 ppmv CO_2, the ocean temperatures increase greatly, especially in the tropics where the warm ocean layer, which has potential temperature higher than 0 °C, extends to below 2,000 m near the equator (Fig. 2*B*). The highest temperature is up to 8 °C, much higher than that of the 355-ppmv case. The increase in ocean temperatures is not only because of much stronger greenhouse effect but also the broader open-ocean area that absorbs more stellar radiation at much lower surface albedo than that of sea ice and snow. Zonal-mean zonal ocean velocities are shown in Fig. 2 *C* and *D*. Both demonstrate equatorial jet streams. As CO_2 increases from 355 to 200,000 ppmv, the equatorial jet stream becomes stronger and expands both downward and poleward. As shown below, the increases in both ocean temperatures and zonal velocities with increasing CO_2 cause more ocean heat transport from the dayside to the nightside. Fig. 2 *B* and *D* display a slight asymmetry between the two hemispheres, which is probably introduced by the time interval (100 Earth years) for averaging, which is not long enough.

Contours overlapped in Fig. 2 *C* and *D* are the mean meridional mass streamfunction of ocean, which represents zonal-mean ocean meridional overturning circulations (MOC). In both plots, streamlines display two layers of circulation cells with opposite directions. The cells in the upper layer (above 300 m) are driven by wind stress. Westerly winds produce an equatorward Ekman drift and therefore descending motion at the equator, and equatorward wind stress drives cold surface water from high latitudes toward the equator for compensation. Equatorial warm water at depth moves poleward and eventually upward at high latitudes in both hemispheres, forming enclosed ocean meridional circulations. The cells in the lower layer, with maximum values of about 1,000 Sv, are the so-called thermohaline circulations that are driven by meridional density contrast due to temperature and salinity differences. Sea-ice formation generates salty water in the cold ice-covered region, while sea-ice melting in the warm open-ocean region freshens ocean water there. Denser water at high latitudes descends and moves equatorward, while lighter water in the tropics rises and moves poleward, forming the thermohaline circulations. These meridional ocean circulations lead to exchanges between warm tropical water and cold high-latitude water and generate net poleward heat transport. In addition to the mean MOCs, eddy-induced MOCs also transport heat poleward, as shown in Fig. S2 *A* and *B*. However, eddy-induced MOCs are about one order weaker than the mean MOCs. As CO_2 is increased, both mean and eddy-induced MOCs become stronger and thus transport more heat from the tropics to high latitudes.

Atmospheric and ocean zonal heat transports from the dayside to the nightside are quantified and compared in Fig. 3. Both atmospheric and ocean zonal heat transports have maximum values at the equator and decrease with latitudes (Fig. 3 *A* and *C*). This is consistent with the fact that both atmospheric and oceanic flows have maximum velocities at the equator. For 3.6 ppmv CO_2, the maximum zonal heat transport by the atmosphere is nearly twice greater than that by the ocean, i.e., 1.2 versus 0.7 PW. In general, atmospheric heat transport decreases with increasing CO_2. In contrast, ocean heat transport increases with increasing CO_2. For 200,000 ppmv CO_2, the maximum ocean heat transport is about twice greater than that by the atmosphere, i.e., 2.0 versus 0.9 PW. The decrease in atmospheric heat transport with increasing CO_2 is because of largely reduced thermal contrast between the dayside and nightside (Fig. 1 *C* and *D*). The increase in ocean heat transports with increasing CO_2 is

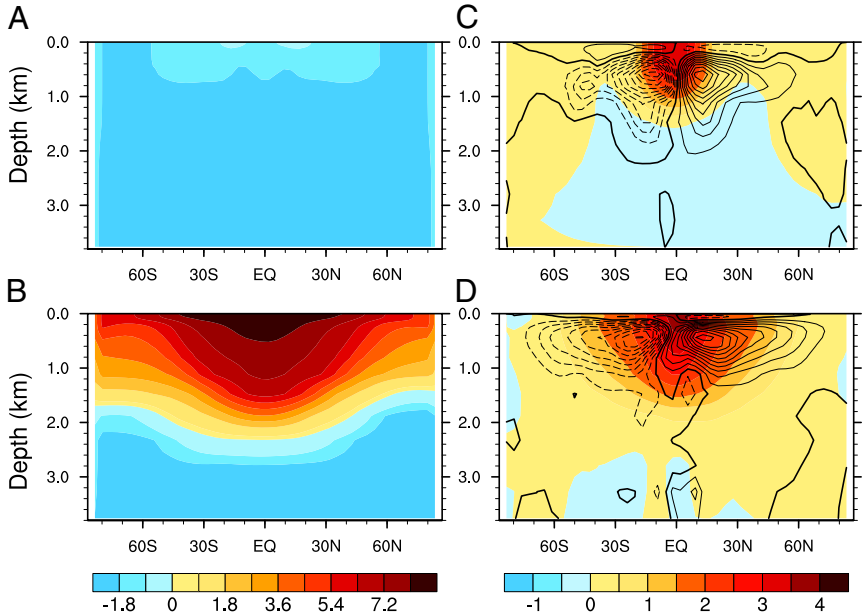

Fig. 2. Depth–latitude cross-sections of zonal-mean ocean potential temperatures and zonal-mean zonal velocity. (*Left*) Ocean potential temperature (unit, °C); (*Right*) ocean zonal velocity (unit, m s^{-1}); (*Upper*) 355 ppmv CO_2; and (*Lower*) 200,000 ppmv CO_2. In *C* and *D*, yellow-red colors indicate westerly flows, blue colors indicate easterly flows, and contours are the mean meridional mass streamfunction. Solid contours indicate clockwise streamlines, and dashed contours are anticlockwise streamlines. Contour interval is 100 Sv.

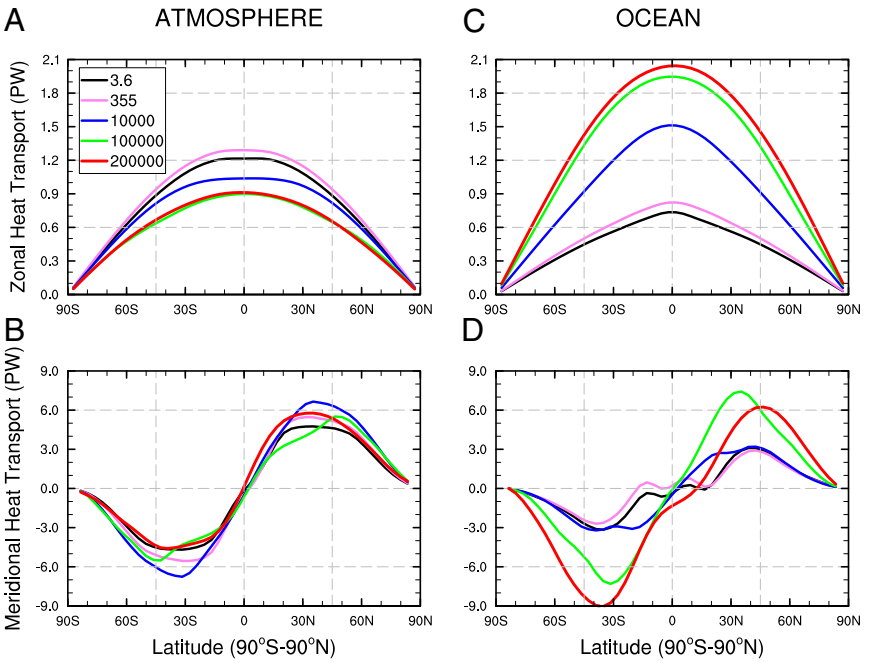

Fig. 3. Vertically integrated zonal and meridional heat transports by the atmosphere and by the ocean from the dayside to the nightside for various CO_2 levels. (*Left*) Atmospheric heat transports; (*Right*) ocean heat transports; (*Upper*) zonal heat transports; and (*Lower*) meridional heat transports. Unit is PW. Zonal energy fluxes here are calculated using the method in ref. 31 We first calculate the net upward energy flux through the ocean surface. Second, we use the net surface energy flux to calculate the vertically integrated divergent ocean heat flux. Then, we use the net downward energy fluxes at both the top of the atmosphere and the surface to calculate the divergent atmospheric energy transport. Zonal energy transport from the dayside to the nightside is the sum of energy fluxes across vertical cross-sections at both vertical cross-sections of both 90° and 270° in longitude.

because of increases in ocean temperatures and zonal velocities as well as downward expansion of ocean layers with warm temperatures and strong zonal velocities, as shown in Fig. 2. Atmospheric and ocean meridional heat transports are plotted in Fig. 3 *B* and *D*, respectively. The maximum values of atmospheric meridional heat transports, located between 30 and 40° in latitude in both hemispheres, range from about 4.5 to about 6.5 PW, which are comparable to that of the Earth's atmosphere [about 3.0 PW (30)]. The maximum ocean meridional heat transports are close to that of Earth oceans [about 2.0 PW (30)] for lower CO_2 levels. For much higher CO_2 levels (e.g., 100,000 and 200,000 ppmv), ocean meridional heat transports are rapidly increased to 6.0–7.0 PW.

Our simulations show that sea-ice thickness is generally thin (Fig. S3). Sea-ice thickness is about 5 m in the coldest regions, less than 3 m on most parts of the dayside, and less than 2 m near the equator. Sea-ice thickness in the coldest regions is less than 10 m even for 3.6 ppmv of CO_2. This largely contrasts with the simulation results without a dynamic ocean, in which sea-ice thickness can grow up to several thousands of meters on the nightside, and the global-mean sea-ice thickness is greater than 500 m (32). Our simulations showed that sea-ice dynamics plays an important role in keeping sea ice thin at the nightside and high latitudes, in addition to ocean heat transports. Such thin sea ice would allow existence of life in not only the open-ocean region but also ice-covered regions on the dayside because stellar radiation can penetrate such thin sea ice and photosynthesis can occur under sea ice.

To further demonstrate how ocean heat transport influences the climate and habitability of tidally locked exoplanets around M stars, we perform AOGCM and AGCM simulations with different stellar radiation fluxes, but with a fixed CO_2 concentration of 355 ppmv. The results are shown in Fig. 4. As stellar radiation is decreased to 700 W m^{-2}, sea-ice coverage reaches 100% in AOGCM (Fig. 4*A*); that is, the exoplanet enters a Snowball state. By contrast, ocean remains open in AGCM until stellar radiation is lowered to 550 W m^{-2}. These results suggest that a dynamic ocean tends to draw the outer edge of the HZ inward. On the other hand, as stellar radiation is increased (the exoplanet is moved closer the star), sea ice retreats much faster in AOGCM than in AGCM (Fig. 4*A*). For 1,400 W m^{-2} of stellar flux, sea ice is completely melted in AOGCM, whereas about 70% sea-ice coverage still remains in AGCM. This is similar to the situation of increasing CO_2. Ocean heat transport can efficiently cause global deglaciation as stellar flux is sufficiently high.

T_s changes with increasing stellar radiation are illustrated in Fig. 4 *B*–*D*. The global-mean and minimum surface air temperatures are higher and increase faster with increasing stellar radiation in AOGCM than in AGCM, whereas the maximum T_s is generally lower until stellar radiation reaches 1,400 W m^{-2}. The difference between the global-mean as well as the minimum T_s and the maximum T_s is because zonal ocean heat transport always tends to cool the dayside and warm the nightside. As stellar radiation is sufficiently strong, however, sea ice is completely melted and global surface temperatures become nearly uniform, similar to that in Fig. 1*D*, and the maximum T_s thus becomes higher in AOGCM than in AGCM (Fig. 4*C*). Consistent with T_s differences between the two types of models, atmospheric water-vapor concentration and the tropopause height are all higher in AOGCM than that in AGCM for sufficiently strong stellar radiation. Cloud albedo has significant effects on causing T_s differences between the two types of simulations, as pointed out in ref. 9. It is found that cloud albedo is lower in AOGCM than in AGCM. This is because ocean heat transport reduces day–night temperature contrast in AOGCM, which consequently leads to weaker convections on the dayside and thus lower cloud albedo. The lower cloud albedo causes higher T_s in AOGCM. Because the ocean module becomes numerically unstable, no AOGCM simulations were carried out for stellar radiation stronger than 1,400 W m^{-2}. Nevertheless, it is expected that water-vapor

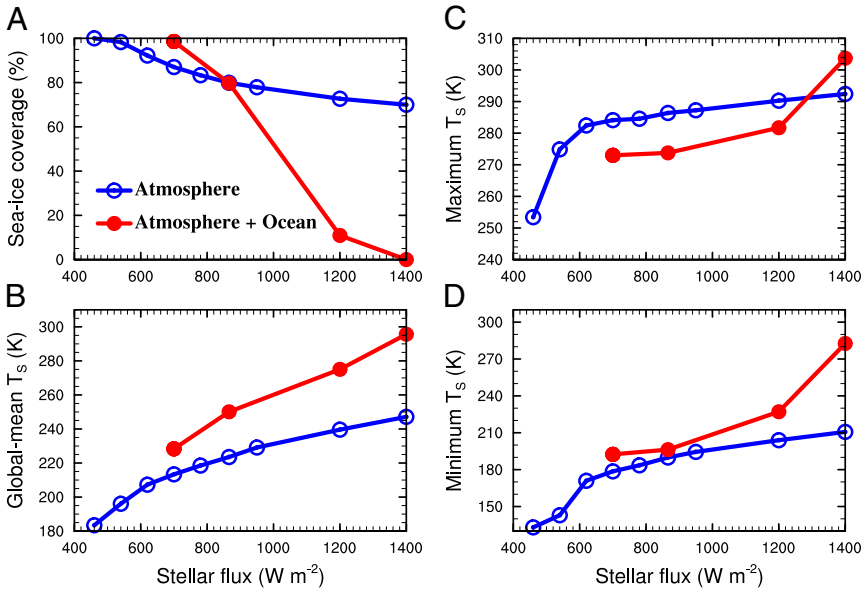

Fig. 4. Comparison of sea-ice coverage and surface air temperatures as a function of stellar radiation fluxes between AOGCM (red) and AGCM (blue). (*A*) Sea-ice coverage; (*B*) global-mean T_s; (*C*) the maximum T_s; and (*D*) the minimum T_s. In both types of simulations, the CO_2 concentration is fixed at 355 ppmv.

concentration and the tropopause height would be higher in AOGCM than in AGCM for stellar radiation stronger than 1,400 W m^{-2}. These results suggest that as a dynamic ocean is considered, an exoplanet would more readily enter the runaway greenhouse state if the exoplanet is close enough to the inner HZ edge and that ocean heat transport likely pushes the inner HZ edge outward.

Discussion and Conclusions

We have demonstrated that ocean heat transports play critically important roles in determining the climate and habitability of tidally locked exoplanets in the HZ around M-type stars. In the presence of a dynamic ocean, the open-ocean area displays a lobster-like spatial pattern, instead of the "eyeball" state. For sufficiently high greenhouse-gas concentrations or strong stellar radiation, ocean heat transport is more efficient than atmospheric heat transport and can cause ice free on the nightside, greatly enlarging the habitable area of tidally locked Super-Earths (but no photosynthesis is possible on the nightside). Sea-ice thickness simulated by AOGCM here is much thinner than that simulated by models without a dynamic ocean. Furthermore, our simulations suggest that a dynamic ocean likely narrows the width of the HZ around M-type stars. The phase shift of surface temperatures between the hottest spots and the substellar point caused by ocean circulations may have observational consequences in both the infrared and visible phase curves of the system, which could be visible in future observational missions.

Exoplanets are likely to have a wide range of ocean depth or even have continents. Results in Fig. 2 suggest that ocean depth has important influences on ocean heat transports because the strong equatorial current and the warm ocean layer can both extend downward to about 2 km for a strong greenhouse effect. Thus, both zonal and meridional ocean heat transports would largely decrease if ocean depth is shallower by one order. On the other hand, if ocean depth is thicker by one order, ocean heat transport would increase. Given that the ocean is separated by continents, especially by meridional continental barriers, continents would block ocean zonal heat transports from the dayside to the nightside. In such a case, the importance of ocean heat transport would be largely reduced, and the climate state would be more like the "eyeball" state although the open-ocean region is not a round area due to ocean heat transports over ocean-domain scales.

In addition to ocean heat transport, ice–albedo feedback and sea-ice dynamics also have contributions to climates of tidally locked exoplanets. Detailed analysis of these effects is beyond the scope of the present paper. We will report them in a separate paper. It is worth pointing out that it is difficult to make a full exploration on how ocean heat transport would alter the HZ width with current general circulation models (GCMs). Defining the outer and inner HZ boundaries involves high levels of CO_2 and water vapor, respectively, and radiation transfer modules of current GCMs are not valid in resolving these problems.

ACKNOWLEDGMENTS. We thank R. T. Pierrehumbert who sharpened our ideas and helped us greatly in revising early drafts of the paper. We also thank D. N. C. Lin for fruitful discussion on this subject. We are grateful to Y. Liu who helped us set up the model. This project was made possible through the support of a grant from the John Templeton Foundation. The funds from the John Templeton Foundation were awarded in a grant to the University of Chicago which also managed the program in conjunction with the National Astronomical Observatories, Chinese Academy of Sciences. This work is also supported by the National Natural Science Foundation of China (41025018) and by the National Basic Research Program of China (973 Program, 2010CB428606).

1. Rodono M (1986) The M-Type Stars, NASA SP-492, eds Johnson H and Querci F (US Govt Print Off, Washington, DC), pp 409–453.
2. Kasting JF, Whitmire DP, Reynolds RT (1993) Habitable zones around main sequence stars. *Icarus* 101(1):108–128.
3. Joshi M, Haberle R, Reynolds R (1997) Simulations of the atmospheres of synchronously rotating terrestrial planets orbiting M dwarfs: Conditions for atmospheric collapse and implications for habitability. *Icarus* 129(2):450–465.
4. Pierrehumbert RT (2011) A palette of climates for Gliese 581g. *Astrophys J* 726:L8.
5. Heng K, Vogt S (2011) Gliese 581g as a scaled-up version of Earth: Atmospheric circulation simulations. *Mon Not R Astron Soc* 415(3):2145–2157.
6. Edson A, Lee S, Bannon P, Kasting J, Pollard D (2011) Atmospheric circulations of terrestrial planets orbiting low-mass stars. *Icarus* 212(1):1–13.
7. Leconte J, et al. (2013) 3D climate modeling of close-in land planets: Circulation patterns, climate moist bistability and habitability. *Astron Astrophys* 554:A69.
8. Showman A, Wordsworth R, Merlis T, Kaspi Y (2013) *Atmospheric Circulation of Terrestrial Exoplanets* (Univ Ariz Press, Tucson, AZ), pp 1–46.

9. Yang J, Cowan N, Abbot D (2013) Stabilizing cloud feedback dramatically expands the habitable zone of tidally locked planets. *Astrophys J* 771:L45.
10. Hu Y, Ding F (2013) Atmospheric circulations and climate of tidal-locking exoplanets. *Sci Sin-Phys Mech Astron* 43(10):1356–1368.
11. Peixoto J, Oort A (1992) *Physics of Climate* (Am Inst Phys, NY), 520 pp.
12. Pierrehumbert R, Abbot D, Voight A, Koll D (2011) Climate of the Neoproterozoic. *Annu Rev Earth Planet Sci* 39:417–460.
13. Yang J, Peltier W, Hu Y (2012a) The initiation of modern "soft Snowball" and "hard Snowball" climates in CCSM3. Part I: The influence of solar luminosity, CO_2 concentration and the sea-ice/snow albedo parameterization. *J Clim* 25(8):2721–2736.
14. Yang J, Peltier W, Hu Y (2012b) The initiation of modern "soft Snowball" and "hard Snowball" climates in CCSM3. Part II: Climate dynamic feedbacks. *J Clim* 25(8):2737–2754.
15. Collins W, et al. (2006) The Community Climate System Model version 3 (CCSM3). *J Clim* 19(11):2122–2143.
16. Gent P, McWilliams J (1990) Isopycnal mixing in ocean circulation models. *J Phys Oceanogr* 20(1):150–155.
17. Vogt S, et al. (2010) The Lick-Carnegie exoplanet survey: A 3.1M-Earth planet in the habitable zone of the nearby M3V star Gliese 581. *Astrophys J* 723:954.
18. Joshi MM, Haberle RM (2012) Suppression of the water ice and snow albedo feedback on planets orbiting red dwarf stars and the subsequent widening of the habitable zone. *Astrobiology* 12(1):3–8.
19. Selsis F, et al. (2007) Habitable planets around the star Gliese 581? *Astron Astrophys* 476(3):1373–1387.
20. Pierrehumbert R (2010) *Principles of Planetary Climate* (Cambridge Univ Press, UK), 680 pp.
21. Pierrehumbert R (2005) Climate dynamics of a hard snowball Earth. *J Geophys Res* 110(D1):D01111, 10.1029/2004JD005162.
22. Hu Y, Yang J, Ding F, Peltier W (2011) Model-dependence of the CO_2 threshold for melting the hard snowball earth. *Clim Past* 7:17–25.
23. Hu Y, Ding F (2011) Radiative constraints on the habitability of exoplanets Gliese 581c and Gliese 581d. *Astron Astrophys* 526:A135.
24. Gill A (1980) Some simple solutions for heat-induced tropical circulation. *Q J R Meteorol Soc* 106(449):447–462.
25. Showman A, Polvani L (2010) The Matsuno-Gill model and equatorial superrotation. *Geophys Res Lett* 37:L18811, 10.1029/2010GL044343.
26. Showman A, Polvani L (2011) Equatorial superrotation on tidally locked exoplanets. *Astrophys J* 738:71–94.
27. Munk W, Palmen E (1951) Note on the dynamics of the Antarctic Circumpolar Current. *Tellus* 3(1):53–56.
28. Charney J, Spiegel S (1971) Structure of wind-driven equatorial currents in homogeneous ocean. *J Phys Oceanogr* 1(3):149–160.
29. Gill AE (1982) *Atmosphere-Ocean Dynamics* (Academic, NY), 662 pp.
30. Trenberth K, Caron J (2001) Estimates of meridional atmosphere and ocean heat transports. *J Clim* 14(16):3433–3443.
31. Trenberth K, Solomon A (1994) The global heat balance: Heat transports in the atmosphere and ocean. *Clim Dyn* 10(3):107–134.
32. Menou K (2013) Water-trapped world. arxiv.org/abs/1304.6472.

Supporting Information

Hu and Yang 10.1073/pnas.1315215111

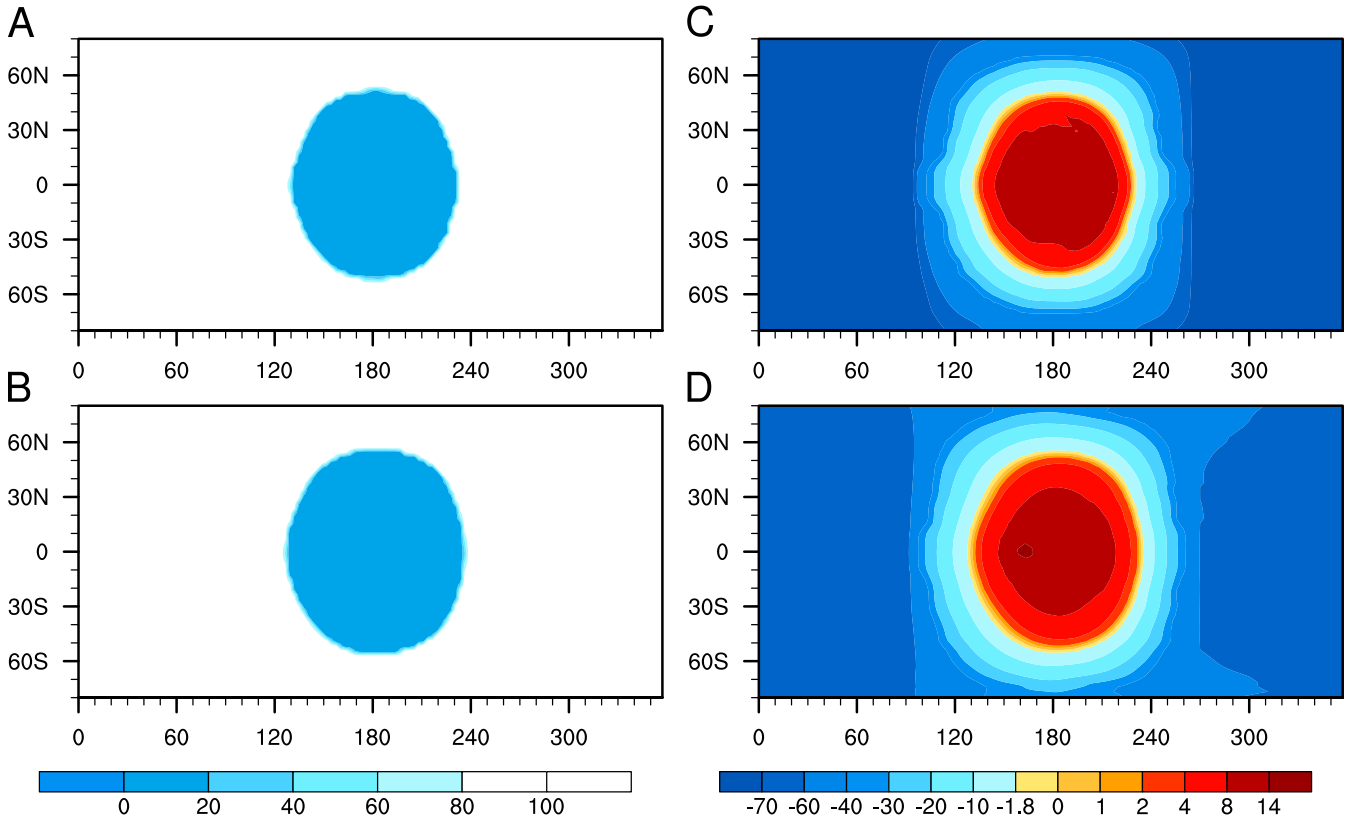

Fig. S1. Sea-ice coverage and surface air temperature in AGCM simulations with a slab ocean. (*Left*) Sea-ice fraction (unit, %); (*Right*) surface air temperature (unit, °C); (*Upper*) 355 ppmv of CO_2; and (*Lower*) 200,000 ppmv of CO_2. For *A* and *B*, blue indicates open ocean, and white indicates sea ice. Note that the color scale is not linear in *C* and *D*.

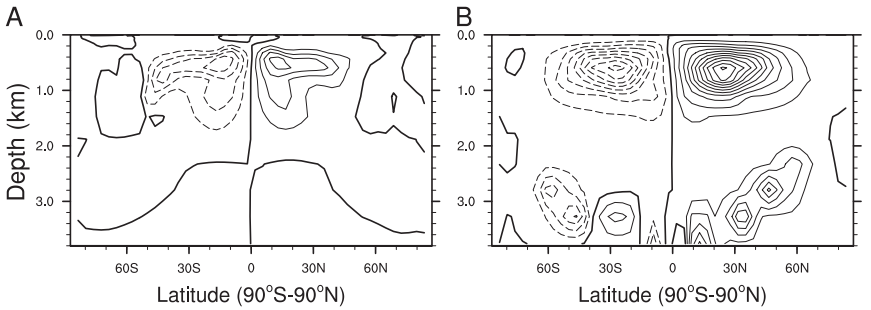

Fig. S2. Mean meridional mass streamfunction of eddy-induced MOCs. Contour interval is 10 Sv. Shown are (*A*) 355 ppmv and (*B*) 200,000 ppmv of CO_2. Solid contours indicate clockwise streamlines, and dashed contours indicate anticlockwise streamlines. The exoplanet studied here has a much slower rotating rate, 36.7 times slower than Earth's. Its gravity is 1.35 times greater than Earth's. Thus, the Rossby radius of deformation of its ocean is about 43 times larger than for Earth's oceans, according to the formula $L_R = (gD)^{1/2}/f_o$ for a barotropic ocean as an example. Here, L_R is the Rossby radius of deformation, g is the gravity, D is the ocean depth, and f_o is the Coriolis parameter at the reference latitude. L_R is about 200 km for Earth's tropical ocean. Thus, L_R is about 8,500 km for the exoplanet studied here, which is much greater than the numerical resolution of the ocean model. Therefore, persistent ocean eddies are model-resolved, and eddies parameterized by the Gent–McWilliams parameterization are weak.

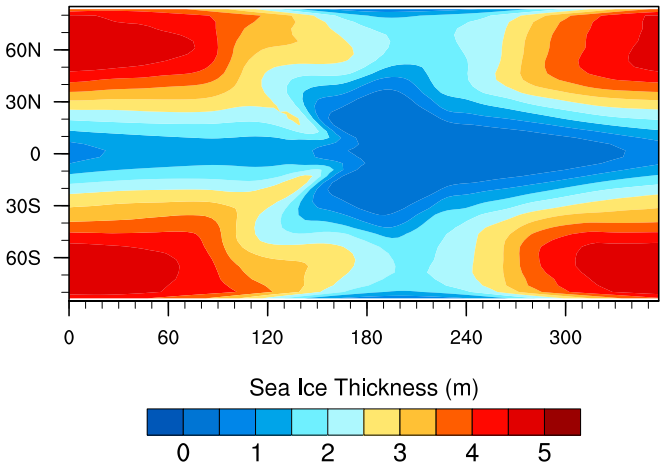

Fig. S3. Sea-ice thickness for 355 ppmv of CO_2. Color interval is 0.5 m.